Dissecting biexciton wave functions of self-assembled quantum dots by double-quantum-coherence optical spectroscopy

Benjamin P. Fingerhut,[1] Marten Richter,[1,2] Jun-Wei Luo,[3] Alex Zunger,[4,*] and Shaul Mukamel[1,†]

[1]*Department of Chemistry, University of California, Irvine, California 92697-2025, USA*

[2]*Institut für Theoretische Physik, Nichtlineare Optik und Quantenelektronik, Technische Universität Berlin, Hardenbergstr. 36, 10623 Berlin, Germany*

[3]*National Renewable Energy Laboratory, Golden, Colorado 80401, USA*

[4]*University of Colorado, Boulder, Colorado 80309, USA*

(Received 24 July 2012; published 5 December 2012)

Biexcitons feature prominently in various scenarios for utilization of quantum dots (QDs) for enhancing the efficiencies of solar cells, and for the generation of entangled photon pairs in single QD sources. Two-dimensional double quantum coherence (2D-DQC) nonlinear optical spectra provide novel spectroscopic signatures of such states beyond global intensity and lifetime characteristics which are available by more conventional techniques. We report the simulation of a prototype 2D-DQC optical experiment of a self-assembled InAs/GaAs dot. The simulations consider the QD in different charged states and are based on a state-of-the-art atomistic many-body pseudopotential method for the calculation of the electronic structure and transition dipole matrix elements. Comparison of the spectra of negatively charged, neutral, and positively charged QD reveals optical signatures of their electronic excitations. This technique directly accesses the biexciton (XX) energies as well as the projections of their wave functions on the single-exciton manifold. These signals also provide a unique tool for probing the charged state of the QD and thus the occupation of the quantum state. Signatures of Pauli blockade of the creation of certain single and two excitons due to charges on the particles are observed. For all quantum states of the QD, the spectra reveal a strong multiconfiguration character of the biexciton wave functions. Peak intensities can be explained by interference of the contributing Liouville space pathways.

DOI: 10.1103/PhysRevB.86.235303 PACS number(s): 78.47.jh, 73.21.La

I. INTRODUCTION

The confined electronic space created by matrix-embedded quantum dots often leads to the association of single excitons into exciton complexes. The existence of such natural complexes has led to the proposal of numerous schemes for their utilization in solar cells[1,2] (multiple excitons generated from a single electron-hole pair via inverse Auger process), quantum computing,[3–11] entangled photons (created from a cascade decay of biexciton and monoexciton)[8,9,11,12] and "on-demand" single photon emitters,[5–7] which realize a light source that, upon a trigger event, emits one and only one photon within a short time interval. Self-assembled dots represent artificial macromolecules of molecular weight $\approx$1 000 000, corresponding, for example, to simple covalent semiconductors such as InAs embedded seamlessly in GaAs matrix.[13,14] As a result of the confinement of both InAs electrons and holes by the GaAs barrier, the electron Coulomb interaction and electron correlations are enhanced in such zero-dimensional (0D) QDs with respect to 2D quantum wells and 1D quantum wires. Such *self-assembled* QDs represent a special case where multiexcitons made of N_e electrons and N_h holes (including neutral $N_e = N_h$ as well as charged multiexcitons) are readily formed and decay radiatively, surviving many of the nonradiative decay channels that rapidly destroy multiexcitons in *colloidal* QDs.[2,15] They are thus a natural laboratory for studying optical and electronic features of interacting excitons. These appear in a series of charged and neutral states as follows: X^q and XX^q correspond to QDs with N_e electrons and N_h holes and charge $q = N_h - N_e$. A neutral monoexciton ($N_h = N_e = 1$) is denoted X^0, positively charged monoexciton ($N_h = 2, N_e = 1$) is X^+ and negatively charged monoexciton ($N_h = 1, N_e = 2$) is X^-, whereas neutral biexciton ($N_h = N_e = 2$) is XX^0, positively charged biexciton ($N_h = 3, N_e = 2$) is XX^+, and negatively charged biexciton ($N_h = 2, N_e = 3$) is XX^-. The transition from the ground state manifold G^q [we considered neutral (no unpaired electron e or hole h (0,0)), negatively charged (an additional unpaired e in the QD (0,1)) and positively charged QD (an additional unpaired h in the QD (1,0))] into the single-exciton manifold X^q generates an additional electron-hole pair in the respective charged QDs, characterized by the transitions $G^0 = (0,0) \rightarrow X^0 = (1,1)$, $G^- = (0,1) \rightarrow X^- = (1,2)$, and $G^+ = (1,0) \rightarrow X^+ = (2,1)$. Accordingly, monoexciton to biexciton transitions appear as $XX^0 = (2,2) \rightarrow X^0 = (1,1)$; $XX^+ = (3,2) \rightarrow X^+ = (2,1)$; $XX^- = (2,3) \rightarrow X^- = (1,2)$ (the charged state q is the same in both monoexciton and biexciton manifolds).

Linear spectra of self-assembled semiconductor QDs show in high resolution, a series of multiexciton transition peaks observed with ultra high resolution with zero-phonon linewidth less than 10 μeV at low temperature (T = 4 K).[16] The absorption and emission spectra of single- and multiexcitons encode information about the Coulomb interactions between carriers, such as exchange and correlation effects and thus reveal many-particle physics in confined spaces.[17] Nevertheless, information about homogeneous widths or two-quantum coherence induced by many-body effects can not be accessed by linear one-dimensional (1D) techniques. Coherent two-dimensional (2D) optical spectroscopic techniques like double quantum coherence (DQC) or photon echo became experimentally feasible in the last decade.[18–21] These can unfold complex and highly congested spectra by spreading them in two dimensions as is done in NMR.[22–24] Third-order

2D spectra carry information about the mono- (X^q) and the biexciton (XX^q) manifold beyond what can be inferred from linear spectroscopy: for example, the 2D-DQC technique correlates biexciton states XX^q to the constituent monoexciton X^q, and thus offers a direct probe of the XX^q energy and composition. The phase relations between interfering quantum pathways of the density matrix define the 2D-DQC signal intensity,[25] beyond the interaction of light with a single transition moment.[26]

In a typical coherent 2D third-order DQC experiment the QD interacts with a sequence of four (femtosecond and phase stable) laser pulses, the first two with wave vectors $\mathbf{k_1}$ and $\mathbf{k_2}$ excite the QD and induce a polarization that oscillates at the frequency of the biexciton manifold XX^q; after a waiting time t_2, the third pulse with wave vector $\mathbf{k_3}$ acts as a probe and deexcites the biexciton manifold XX^q to the single exciton manifold X^q. The fourth pulse $\mathbf{k_4}$ is used for heterodyne detection, which allows to record frequency, amplitude and phase information of the optical high frequency signal. The 2D-DQC technique offers the advantage that the biexciton energies XX^q show up directly as resonances along the Ω_2 axis and are thus directly accessible. Due to the third interaction $\mathbf{k_3}$ the XX^q states are projected on the X^q manifold along the Ω_3 axis giving a direct probe of the XX^q-X^q correlations.[27,28] This feature of 2D-DQC reveals high-order electron and hole correlations not accessible by linear spectroscopy. The temporal control of the pulses and detection of the signal $S^{(3)}_{k_{\rm III}}$ in the direction $\mathbf{k}_{\rm III} = +\mathbf{k_1} + \mathbf{k_2} - \mathbf{k_3}$ reduces the number of contributing Liouville space pathways to two purely excited state absorption (ESA) type contributions compared to frequency domain techniques.[16,22,29,30] Compared to other coherent 2D third-order techniques, like, e.g., the photon echo technique, the DQC technique has the advantage that the biexciton energies XX^q are directly accessible, whereas in photon echo spectroscopy excited state emission and ground-state bleach contribute to the signal together with excited state absorption components. In bulk assemblies of QDs, the $\mathbf{k}_{\rm III}$ signal can be observed in the direction $+\mathbf{k_1} + \mathbf{k_2} - \mathbf{k_3}$ (phase matching condition). Single-dot signals are isotropic. Nevertheless, the $\mathbf{k}_{\rm III}$ signal can be extracted by using a wave guide geometry[16] and by repeating the experiment several times with different phases φ_l of the various pulses. This procedure, commonly used in 2D-NMR, is known as phase cycling.

Alternatively, the detection of emission induced by a sequence of four phase controlled pulses yields similar information about quantum pathways[31–35] in ensembles[33,34,36,37] and even in single molecules.[38] This alternative DQC phase modulated fluorescence (DQC-PM-Fl) experiment contains comparable information as obtained from the third-order coherent technique DQC, a detailed deviation can be found in Ref. 35. In PM-Fl techniques, one additional ladder diagram contributes to the fourth-order signal, moreover, the signs of the interfering pathways vary.[34] In an ideal coherent DQC-PM-Fl experiment, the quantum yield of photon emission from the XX^q state reaches a value of two ($|XX^q\rangle \rightarrow |X^q\rangle \rightarrow |G^q\rangle$) and no nonradiative decay (like nonradiative Auger decay) of the XX^q biexciton manifold occurs. In this case, the DQC-PM-Fl signal with phase $\Phi_{\rm III} = \phi_1 + \phi_2 - \phi_3 - \phi_4$ equals the third-order DQC signal. Unavoidable nonradiative decay processes lead to differences in the DQC-PM-Fl and third-order DQC spectra and reveal information about the XX^q population and quantum yield. Due to the unique photoluminescence properties of QDs,[39] DQC-PM-Fl may serve as a promising alternative to third-order coherent techniques, the spectrally resolved ESA contributions of the 2D-DQC signal of the QDs would allow to record the different pathways independently.

Here, we report the theoretical simulation of the 2D-DQC signal of single InAs/GaAs QD carrying different charges. Such dots contain a few million atoms (dot + matrix) so their electronic structure requires special techniques. For the electronic structure of the QD, we use a high-level atomistic many-body pseudopotential method.[17,39–43] We will demonstrate that the DQC technique provides a sensitive tool for characterizing the charged state. We observe clear signatures of Pauli-blocking due to partially occupied electron or hole states in the charged QD. Furthermore, the 2D-DQC signal reveals correlations between excitons (also called high-order electron correlations), which are impossible to observe in linear spectroscopy allowing the analysis of XX^q states with regard to their constituent X^q manifold. In all different quantum states, the spectra reveal strong electron correlation due to geometric confinement within the dot, evidenced by the fact that the energy of XX^q states is reduced with respect to the sum of contributing X^q states. The characteristic X^q manifold pattern reflects the multiconfiguration character of the XX^q wave functions. Peak intensities are explained by the interference of the contributing quantum pathways beyond a simple transition dipole analysis.

II. THEORETICAL METHODS

A. Atomistic many-body calculations

As specific system we consider a lens-shaped InAs/GaAs self-assembled QD with a circular base size of 25-nm diameter and 2-nm height sitting on one monolayers of "wetting layer" [see Fig. 1(a)]. It contains 41 776 atoms and the matrix contains 1 948 880 atoms. The lattice mismatch between InAs and GaAs induces a built-in strain in the InAs/GaAs dot. An atomistic valence force field model is used to relax the atomic position $\mathbf{r}$ in order to minimize the strain energy.[42] Given the relaxed atomic positions, we calculate the energy levels and wave functions using atomistic many-body pseudopotential method[40,42,43] in two steps. The first step is to obtain single-particle approximated (without many-body interaction) energy levels $\{\epsilon_i\}$ and wave functions $\{\Phi_i(\mathbf{r})\}$ by solving the Schrödinger equation of crystal (dot+matrix) potential $V(\mathbf{r})$ in a linear combination of bulk bands method.[41,42] The screened potential $V(\mathbf{r})$ is described as a superposition of overlapping atomic (pseudo) potentials centered at the atomic positions: $V(\mathbf{r}) = \sum_n \sum_\alpha \hat{v}_\alpha(\mathbf{r} - \mathbf{R}_n - \mathbf{d}_\alpha)$, where $\hat{v}_\alpha(\mathbf{r} - \mathbf{R}_n - \mathbf{d}_\alpha)$ pertains to atom type α at site $\mathbf{d}_\alpha$ in the nth primary cell $\mathbf{R}_n$. Thus the correct atomically resolved symmetry is retained for the eigenstates.[44–46] The atomic potentials $\hat{v}_\alpha$ were empirically fit to experimental bulk quantities:[42] transition energies, spin-orbit splittings, effective masses, and deformation potentials as well as the band offsets of two materials in a heterostructure. This approach cures

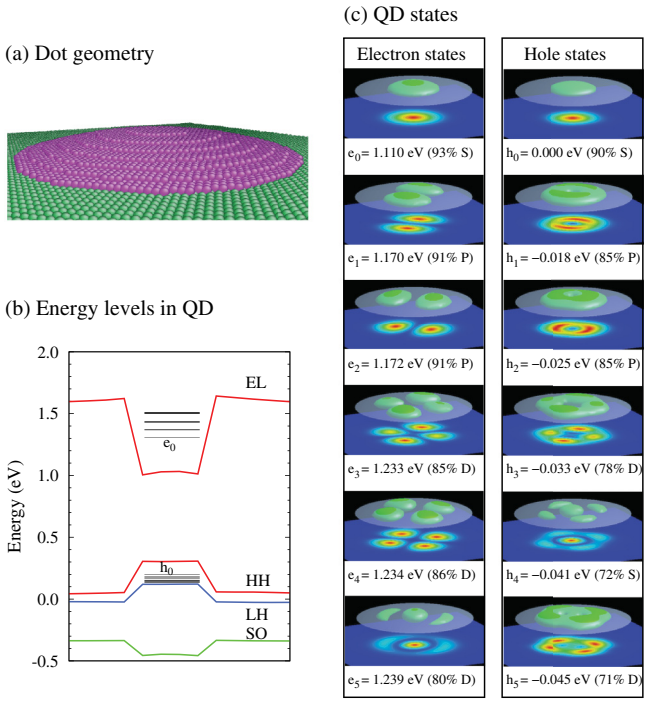

FIG. 1. (Color online) (a) Schematic of a lens-shaped InAs dot with base of 25 nm and 2 nm heigh, sitting on one monolayer wetting layer, embedded in a GaAs matrix. The dot contains 41 776 atoms and the matrix contains 1 948 880 atoms. (b) The corresponding strain modified band edge alignment of electron band (EL), heavy-hole (HH), light-hole (LH), and spin-orbit split (SO) bands. The atomistic pseudopotential method calculated lowest 10 electron ($e_0, e_1, \ldots, e_9$) and top 10 hole ($h_0, h_1, \ldots, h_9$) levels of the QD are shown in black lines. (c) Wave-function square of six lowest energy single-particle electron states and six highest hole states. The percentage of its dominant orbital character (S, P, and D) and its energy with respect to h_0 are given underneath the corresponding wave-function plot.

the well-documented DFT band gap and effective mass errors and captures the multiband and intervalley couplings. The wave functions are expanded by a set of plane waves with a small energy cutoff $E_{\text{cut}} = 5$ Ry (68.03 eV). The solved single-particle QD states are shown in Figs. 1(b) and 1(c): the ground electron state e_0 is S-like followed by two P-like and three D-like electron states, whereas the S-like ground hole state h_0 is followed by two P-like and then one S-like state inserts into the three D-like states. The reduced weight of the dominant orbital contribution (S, P, and D) of hole states (compared to the respective electron states) shows that the interorbital (e.g., S-P) coupling is stronger in hole states than in electron states.

The second step is to calculate the many-body excitonic states $\{\epsilon_i, \Psi_i\}$ using a screened configuration interaction (CI) method[40] in a basis set of Slater determinants $\{\Phi_{v,c}\}$ constructed from 12 electron and 12 hole single-particle states (including spin) for the InAs/GaAs QD. The electron correlations, which play a predominant role in multidimensional quantum coherent spectra, are taken into account by the configuration interaction. The interaction consists of electron-hole (e-h) Coulomb interaction (binding the e-h pair and thus forming the exciton) and e-h exchange interaction (splitting symmetry-different exciton states). The many-body exciton problem is set up in a basis set of Slater determinants as a CI expansion,[40]

$$\langle \Phi_{v,c}|H|\Phi_{v',c'}\rangle = (\epsilon_c - \epsilon_v)\delta_{v,v'}\delta_{c,c'} - J_{vc,v'c'} + K_{vc,v'c'}, \tag{1}$$

where J and K are the Coulomb and exchange integrals:

$$J_{vc,v'c'} = \sum_{\sigma_1,\sigma_2} \iint \frac{\Psi_v^*(\boldsymbol{r}_1,\sigma_1)\Psi_c^*(\boldsymbol{r}_2,\sigma_2)\Psi_{v'}(\boldsymbol{r}_1,\sigma_1)\Psi_{c'}(\boldsymbol{r}_2,\sigma_2)}{\bar{\epsilon}(\boldsymbol{r}_1,\boldsymbol{r}_2)\,|\boldsymbol{r}_1 - \boldsymbol{r}_2|} \times d\boldsymbol{r}_1 d\boldsymbol{r}_2, \tag{2}$$

$$K_{vc,v'c'} = \sum_{\sigma_1,\sigma_2} \iint \frac{\Psi_v^*(\boldsymbol{r}_1,\sigma_1)\Psi_c^*(\boldsymbol{r}_2,\sigma_2)\Psi_{c'}(\boldsymbol{r}_1,\sigma_1)\Psi_{v'}(\boldsymbol{r}_2,\sigma_2)}{\bar{\epsilon}(\boldsymbol{r}_1,\boldsymbol{r}_2)\,|\boldsymbol{r}_1 - \boldsymbol{r}_2|} \times d\boldsymbol{r}_1 d\boldsymbol{r}_2. \tag{3}$$

The size-dependent screening function $\bar{\epsilon}(r)$ for Coulomb and exchange integrals is calculated following the microscopic model of Resta[40] and exhibits a smooth transition from unscreened at short range to screened at long range. This approach naturally includes both long- and short-range exchange.[47,48] Once the many-body wave functions of multiexcitons are solved from above equations, the dipole transition matrix elements will be readily obtained. The linear absorption spectra, calculated according to Fermi's golden rule with a broadening parameter $\gamma = 1$ meV, of transitions $G^0 = (0, 0) \rightarrow X^0 = (1, 1)$, $G^- = (0, 1) \rightarrow X^- = (1, 2)$, and $G^+ = (1, 0) \rightarrow X^+ = (2, 1)$ are shown in Figs. 2(a)–2(c), respectively. Earlier calculations of photoluminescence spectra for different exciton charges of this QD reproduce well the experimental measurement by Warburton's group.[39]

B. 2D double quantum coherence (2D-DQC) spectra

The simulation of the 2D-DQC spectra starts with the construction of an effective three band exciton Hamiltonian, used for the calculation of the third-order optical response. The relevant exciton states accessed by the 2D-DQC technique are the ground-state manifold G^q, the single-exciton manifold X^q as well as the biexciton manifold XX^q (with $q = 0, +$, and $-$ for the neutral, positively charged, and negatively charged QD, respectively). The three different manifolds of states, obtained from the atomistic many-body calculations upon diagonalization of the CI Hamiltonian are connected by the respective dipole transition matrix elements $\mu_{i,j}$. The total Hamiltonian has the form

$$H = H_0 + H_{eL}, \tag{4}$$

$$H_0 = \sum_{G^q} \varepsilon_{G^q}|G^q\rangle\langle G^q| + \sum_{X^q} \varepsilon_{X^q}|X^q\rangle\langle X^q| + \sum_{XX^q} \varepsilon_{XX^q}|XX^q\rangle\langle XX^q|, \tag{5}$$

$$H_{eL} = \sum_{G^q,X^q} E(t)\cdot\mu_{G^q,X^q}|G^q\rangle\langle X^q| + \sum_{X^q,XX^q} E(t)\cdot\mu_{X^q,XX^q}|X^q\rangle\langle XX^q| + \text{c.c.}, \tag{6}$$

where H_0 describes the isolated dot and H_{eL} is the interaction between quantum states of the isolated dot with the optical

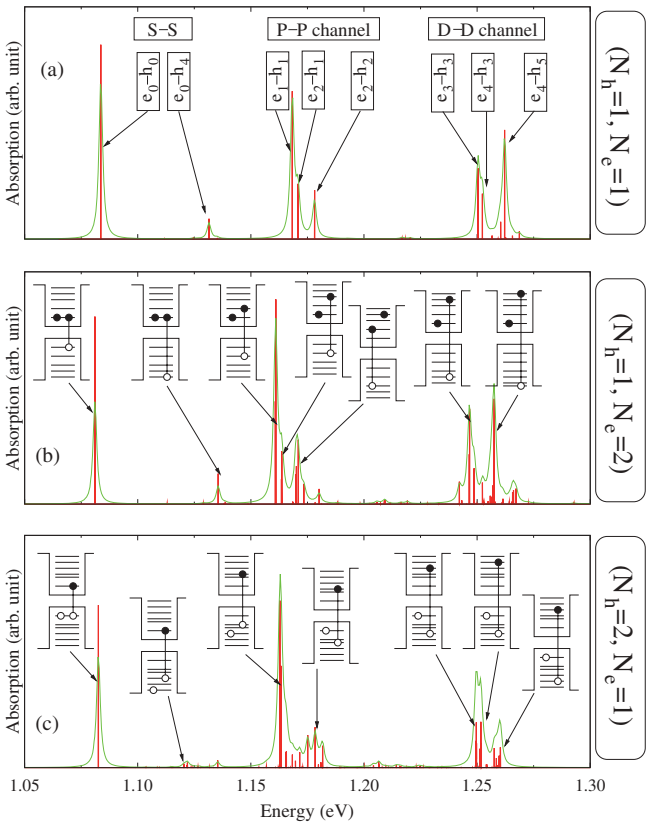

FIG. 2. (Color online) Many-body atomistic pseudopotential method calculated linear absorption spectra of the InAs/GaAs dot: (a) $G^0 = (N_h = 0, N_e = 0) \rightarrow X^0 = (N_h = 1, N_e = 1)$, (b) $G^- = (N_h = 0, N_e = 1) \rightarrow X^- = (N_h = 1, N_e = 2)$, and (c) $G^+ = (N_h = 1, N_e = 0) \rightarrow X^+ = (N_h = 2, N_e = 1)$ transitions. The inserts show the corresponding dominant configuration of main peaks.

field. In the case of negatively or positively charged QDs, the ground-state manifold G^q has several states, in all simulations we assume that the QD is initially in the lowest-energy state G_0^q. The energy range of the X^q and XX^q manifold is chosen to cover the energy range of the $P_e - P_h$ channel ($\varepsilon_{X^q,\max} = 1.19$ eV, see below Fig. 2) for $G^q \rightarrow X^q$ transitions and $\varepsilon_{XX^q,\max} \approx 2.31$ eV for the $G^q - XX^q$ total energy range. In total, we consider 144 X^0 and 4356 XX^0 states, 500 X^+ and X^- and 1000 XX^+ and XX^- states. Together with the considered G^q manifold (12 states), this gives rise to 6×10^7 different transitions for the calculation of the 2D-DQC signal.

We consider a time-domain 2D-DQC experiment where a sequence of four (femtosecond and phase stable) laser pulses (E_1, E_2, E_3, and E_4) interacts with the QD [see Fig. 3(a,i)], the first pulse E_1 excites the QD into a $|X^q\rangle\langle G^q|$ coherence of the density matrix during the waiting time t_1; the second pulse E_2 accesses the biexciton manifold XX^q and creates a $|XX^q\rangle\langle G^q|$ coherence during t_2 [see Fig. 3(a,ii)]. The third pulse E_3 acts as a probe, projecting the biexcitons XX^q on the single exciton manifold X^q, the fourth pulse E_4 is used for heterodyne detection, which allows to record frequency, amplitude, and phase information of the optical signal $S^{(3)}_{k_{\rm III}}(t_3,t_2,t_1)$. The temporal control of the pulses and the phase matching condition $\mathbf{k}_{\rm III} = +\mathbf{k_1} + \mathbf{k_2} - \mathbf{k_3}$ reduces the number of contributing pathways to two excited state absorption (ESA) type contributions:[24]

$$S^{(3)}_{k_{\rm III}}(t_3,t_2,t_1) = S^{(\rm ESA1)}_{k_{\rm III},i}(t_3,t_2,t_1) - S^{(\rm ESA2)}_{k_{\rm III},ii}(t_3,t_2,t_1). \quad (7)$$

Both ladder diagrams are depicted in Figs. 3 (a,iii) and 3(a,iv). The signal $S^{(3)}_{k_{\rm III}}(t_3,t_2,t_1)$ depends on three controlled delay periods t_1, t_2, t_3. The frequency domain 2D-DQC signal is obtained by a double Fourier transform with respect to two time intervals holding the third fixed. Since the most interesting biexciton dynamics is contained in t_2, we chose to correlate it either with t_1 [$S^{(3)}_{k_{\rm III}}(t_3,\Omega_2,\Omega_1)$] or with t_3 [$S^{(3)}_{k_{\rm III}}(\Omega_3,\Omega_2,t_1)$]. The $S^{(3)}_{k_{\rm III}}(\Omega_3,\Omega_2,t_1)$ signal with fixed t_1 and transformed t_2 and t_3 to Ω_2 and Ω_3 is easier to measure since it only requires to scan a single delay (t_2), the t_3 information is revealed by dispersion in a spectrometer. The 2D-DQC technique offers the advantage that the biexciton energies XX^q show up directly as resonances along the Ω_2 axis and are thus directly accessible.[28] Due to the third interaction $\boldsymbol{k_3}$ the XX^q states are projected on the X^q manifold along the Ω_3 axis.

The 2D-DQC signals $S^{(3)}_{k_{\rm III}}(t_3,\Omega_2,\Omega_1)$ and $S^{(3)}_{k_{\rm III}}(\Omega_3,\Omega_2,t_1)$ are simulated using sum-over-states expressions of the third-order nonlinear response[23,27] (expressions are given in the Appendix). The signals involve the summation over all possible transitions between the different blocks of the three band exciton Hamiltonian H_0, namely, from the ground-state manifold G^q to the single-exciton manifold X^q, and from X^q to the biexciton manifold XX^q. All transitions are weighted by the respective transition matrix elements μ_{G^q,X^q} and μ_{X^q,XX^q}. The same phenomenological dephasing linewidth of $\gamma = 1$ meV as used in the calculation of linear spectroscopy is assumed for all exciton transitions, reflecting the width of sidebands of the QDs due to acoustical phonons[16,49–52] and the similar radiative exciton lifetimes of single- and biexcitons in single QD.[53,54] In contrast to colloidal QDs, in single self-assembled QD, the inhomogenous broadening is absent[49] and thus neglected in the calculations. If required, it can be added subsequent to the calculation of the third-order response function.[55] In all calculated spectra, we assume that the bandwidth of the laser pulses is broader than the exciton band (exciton bandwidth from $S_e - S_e$ to $P_e - P_e$ is on the order of 100 meV). To acquire this bandwidth, the required laser pulses have to be shorter than 18 fs (FWHM), centered around 1.12 eV (1107 nm). The broad bandwidth allows us to cover a large area of contributing exciton states and to reveal the relevant physical correlation between them in a single measurement. However, the same information can be obtained by a series of measurements with narrower bandwidth and various color pulses.

III. RESULTS AND DISCUSSION

A. Optical absorption spectra of neutral and charged QDs

Figure 2(a) depicts the stick spectrum together with absorption spectrum of the transition $G^0 = (0,0) \rightarrow X^0 = (1,1)$ in a neutral QD. The corresponding spectra of the negatively charged [$G^- = (0,1) \rightarrow X^- = (1,2)$] and positively charged QD [$G^+ = (1,0) \rightarrow X^+ = (2,1)$] are shown in Figs. 2(b) and 2(c). In the energy range $\omega = 1.05$–1.32 eV, the neutral QD absorption spectrum shows several resonances, which can be characterized by the angular momentum of the

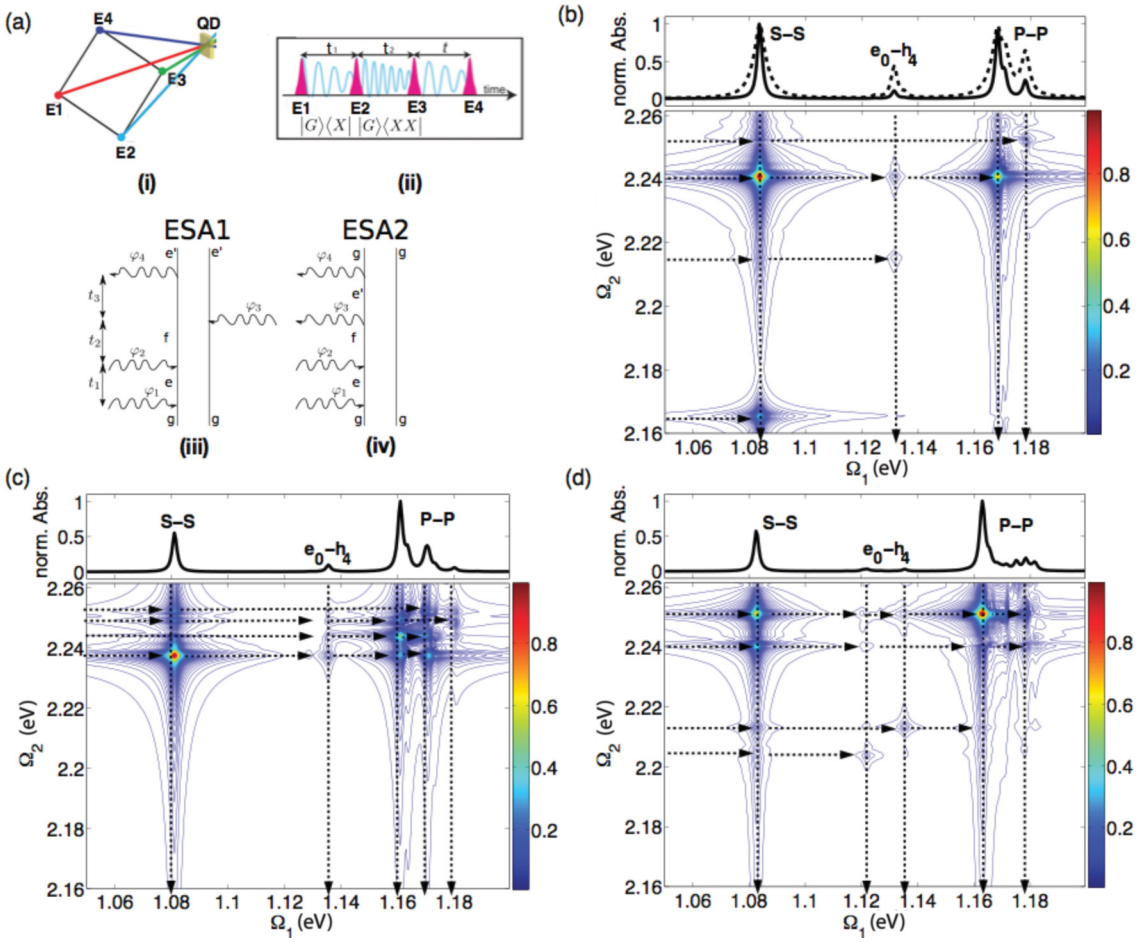

FIG. 3. (Color online) (a) Schematic of a 2D double quantum coherence (DQC) experiment: in (i) the phase matching direction of the pulses is indicated. (ii) Successive interactions induce a polarization in the QD, which oscillates at the frequencies of $|X^q\rangle\langle G^q|$ and $|XX^q\rangle\langle G^q|$ coherences during the waiting times t_1 and t_2. (iii) and (iv) Relevant ladder diagrams for the 2D-DQC signal. (b)–(d) Simulated 2D double quantum coherence signals $S^{(3)}_{k_{III}}(t_3,\Omega_2,\Omega_1)$ of a neutral (b), negatively (c), and positively charged quantum dot (d). The DQC signal is depicted as absolute value on a nonlinear scale defined by Eq. (8) [see dashed line in (b)], $t_3 = 100$ fs.

envelope wave functions. The dominant orbital configuration of the many-body CI states to an electron-hole state $e_i - h_j$ are presented in Fig. 1(c), sorted with increasing angular momentum of the envelope wave functions of electron e_i and hole states h_j.

The lowest energy exciton transition ($\omega = 1.08$ eV) consists of the single-exciton $S_e - S_h$ channel, where both electron and hole states have spherical symmetry ($e_i - h_j = e_0 - h_0$). Due to the additional spin degree of freedom and the spin selection rule this transition is double degenerate. This channel corresponds to transitions between states with S-like wave functions [see Fig. 1(c), top]. The exciton $P_e - P_h$ channel ($\omega = 1.16$–1.18 eV) consists of two orthogonal P-like states in both electron and hole [see Fig. 1(c), middle]. Additionally, two-fold degeneracy due to the spin has to be taken into account. The higher energy, symmetry allowed $D_e - D_h$ channel splits into three main peaks in the linear absorption spectrum [$\omega = 1.24$–1.27 eV, Fig. 1(c), bottom], which are composed of $e_3 - h_3$, $e_4 - h_3$, and $e_4 - h_5$ transitions, respectively. The transition $e_i - e_j = e_0 - h_4$; ($\omega = 1.13$ eV) lies between the $S_e - S_h$ and $P_e - P_h$ states and shows only weak transition strength.

In both, the negatively charged QD [$G^- = (0,1) \rightarrow X^- = (1,2)$] [see Fig. 2(b)] and the positively charged QD [$G^+ = (1,0) \rightarrow X^+ = (2,1)$] [see Fig. 2(c)] the oscillator strength of the lowest energy $S_e - S_h$ transition is reduced compared to $P_e - P_h$. The number of possible transitions is reduced by a factor of two relative to the neutral QD. The additional electron in the negatively charged QD ($0h,1e$) occupies one of the spin degenerate e_0 states, in the positively charged QD ($1h,0e$) the additional hole occupies one of the two spin degenerate S-like h_0. The transitions of the $e_0 - h_4$ channel are shifted towards higher energies in the negatively charged QD ($\Delta\omega = 0.02$ eV), in the positively charged QD the $e_0 - h_4$ transitions are split into two weak resonances [see Fig. 2(c)]. The $P_e - P_h$ and $D_e - D_h$ transitions with doublet structure in the neutral QD are split into several different states in the negatively and positively charged QD. Due to the odd population pattern of electron or hole states in the charged QDs the degeneracy of the exciton states is lifted and several distinct exciton states contribute to the absorption. For all three different quantum states of the QD, we note that only a few discrete states out of the joint density of states of a strongly anharmonic oscillator contribute to the linear absorption. Of all possible $G^q \rightarrow X^q$

transitions (144 for X^0 and 500 for $X^{+/-}$) only a few posses substantial transitions strength due to the selection rules of QD transitions.[56]

B. 2D double quantum coherence (2D-DQC) spectra of neutral and charged QDs

The 2D-DQC technique correlates biexciton states XX^q to the constituent monoexciton X^q and thus offers a direct probe of the XX^q energy and composition. We start with the $S^{(3)}_{k_{III}}(t_3,\Omega_2,\Omega_1)$ signal that shows $|X^q\rangle\langle G^q|$ resonances along Ω_1 and $|XX^q\rangle\langle G^q|$ resonances along Ω_2. Accordingly, the X^q doorway states to a specific XX^q state and the high-order correlations between the X^q monoexcitons are revealed.

The absolute value of $S^{(3)}_{k_{III}}(t_3,\Omega_2,\Omega_1)$ signals of the neutral ($q=0$), the negatively charged ($q=-$) and the positively charged ($q=+$) QD are depicted in Figs. 3(b)–3(d) in the energy range 1.05 eV $<\Omega_1<$ 1.20 eV and 2.16 eV $<\Omega_2<$ 2.26 eV. Horizontal dashed lines indicate a specific biexciton resonance XX^q, whereas respective vertical dashed lines indicate the projection on the single-exciton axis. The signals are depicted on a nonlinear scale:

$$\text{arcsinh}(\mathbb{S}) = \ln(\mathbb{S}+\sqrt{1+\mathbb{S}^2}), \tag{8}$$

with $\mathbb{S}=10\text{abs}(S)/S^{(N)}$, where $S^{(N)}$ is a real normalization constant and S correspond to the 2D-DQC signal $S^{(3)}_{k_{III}}$ on the linear scale. This representation highlights both weak and strong signal components since it interpolates between a linear and a logarithmic scales. In Fig. 3(b), top the nonlinear signal intensity arcsinh($\mathbb{S}$) is depicted as a dashed line and compared with the linear scale for the absorption signal of the neutral QD.

For the neutral QD [see Fig. 3(b)], four $XX^0=(2,2)$ resonances along the Ω_2 axis are identified in the investigated energy range. The lowest-energy XX^0 resonance at $\Omega_2=$ 2.165 eV shows contributions only from the S_h-S_e channel along the Ω_1 axis reflecting the two-fold degeneracy of this state. Accordingly, the XX^0 state composition arises from the product of two S-like $X^0=(1,1)$ excitons. A comparison with the charged QDs [see Figs. 3(c) and 3(d)] shows that this lowest energy XX^0 resonance only appears in the neutral QD. The single electron (hole) in the S configuration of the charged QDs induces a Pauli blockade and prohibits the creation of the $XX^-=(2,3)$ and $XX^+=(3,2)$ only from the S_h-S_e channel. For the neutral QD, the weak XX^0 resonance at $\Omega_2=2.215$ eV shows contributions from the e_0-h_4 channel and the S-like X^0 excitons. The composition of the prominent XX^0 resonance at $\Omega_2=2.241$ eV is more complex with contributions from S_e-S_h, e_0-h_4, and P_e-P_h channels revealing the multiconfiguration character of this XX^0 wave function and the strong high-order electron correlations. The highest-energy XX^0 state with low intensity ($\Omega_2=2.25$ eV) arises from contributions of the high-energy duplet of the P_e-P_h and the S_e-S_h transitions.

For the negatively charged QD, the lowest energy XX^- resonance ($\Omega_2\approx 2.24$ eV) shows contributions from the S_e-S_h, the e_0-h_4 and the P_e-P_h channels. Compared to the neutral QD, the XX^{-1} resonance is shifted towards lower Ω_2 frequencies (2.237 versus 2.241 eV). In the negatively charged QD, the single-exciton X^{-1} configuration of the S_e-S_h channel is dominant, whereas in the neutral dot single-exciton X^0 configurations of the S_e-S_h and P_e-P_h channels contribute with similar magnitude. At higher energies ($\Omega_2\approx 2.25$ eV), two additional XX^- resonances show up in the negatively QD arising predominantly from the P_e-P_h channels, S_e-S_h contributions are minor.

A characteristic signature is found for the positively charged QD [see Fig. 3(d)] due to the splitting of the e_0-h_4 channel, leading to a duplet of XX^{+1} states ($\Omega_2\approx 2.21$ eV) with additional contributions from S_e-S_h. At higher energies ($\Omega_2=$ 2.24–2.26 eV), two prominent XX^{+1} states with strong multiconfiguration character of single excitons X^{-1} from the P_e-P_h, e_0-h_4, and S_e-S_h channels appear. From the above discussion, we have demonstrated that the 2D-DQC spectra of neutral, negatively and positively charged QDs allow to distinguish uniquely between the quantum states of the QD by the presence and composition of the XX^q resonances.

In the $S^{(3)}_{k_{III}}(\Omega_3,\Omega_2,t_1)$ signal, both $|XX^q\rangle\langle X'^q|$ and $|X'^q\rangle\langle G^q|$ coherences are contained along the Ω_3 axis, which complicates the spectra and analysis. Complementary information about the biexcitons is contained in the (Ω_3,Ω_2) spectra.[18] The 2D-DQC signal $S^{(3)}_{k_{III}}(\Omega_3,\Omega_2,t_1)$ is depicted for the neutral, the negatively charged and the positively charged QD in Figs. 4(b)–4(d), respectively. Here, along Ω_3 monoexciton transitions ($|G^q\rangle\rightarrow|X^q\rangle$) together with mono to biexciton transitions ($|X^q\rangle\rightarrow|XX^q\rangle$) are revealed. The additional information contained in this signal representation becomes evident from the photoluminescence of the monoexciton X^q and biexciton XX^q channels of the QDs [see Fig. 4(a)]. The emission occurs from the ground state of either X^q or XX^q states, respectively. The detuning of the transition $|XX^q\rangle\rightarrow|X^q\rangle$ with respect to $|X^q\rangle\rightarrow|G^q\rangle$ reveals partial information about the XX^q manifold of the QDs [see black, red, and blue lines in Fig. 4(a)]. In the 2D-DQC signal, the QD density matrix is in a $|XX^q\rangle\langle X^q|$ or $|X^q\rangle\langle G^q|$ coherence during t_3 [see diagrams (i) and (ii) in Fig. 3(a)]. Accordingly, both ω_{XX^q,X^q} and ω_{X^q,G^q} resonances appear along the Ω_3 axis of the $S^{(3)}_{k_{III}}(\Omega_3,\Omega_2,t_1)$ signal, the contribution of states is not restricted to the ground state of the XX^q, X^q, and G^q manifold, just by the laser pulse bandwidth. The detuning from the $|X^q\rangle\rightarrow|G^q\rangle$ fundamentals is reflected in the $|XX^q\rangle\rightarrow|X^q\rangle$ resonances. The horizontal dashed lines in Figs. 4(b)–4(d) indicate a specific biexciton resonance XX^q. The respective black vertical dashed lines indicate the projection on the monoexciton axis revealing the $|X^q\rangle\rightarrow|G^q\rangle$ contributions, whereas red vertical dashed lines highlight the $|XX^q\rangle\rightarrow|X^q\rangle$ contributions to $S^{(3)}_{k_{III}}(\Omega_3,\Omega_2,t_1)$.

In the neutral QD [see Fig. 4(b)], we identify a minor shift and peak shape asymmetry for the lowest energy XX^0 ($\Omega_2=$ 2.165 eV) along the Ω_3 axis due to a detuning of the S_e-S_h $(2,2)\rightarrow(1,1)$ channel from the S_e-S_h $(1,1)\rightarrow(0,0)$ fundamental transitions. The prominent XX^0 resonance ($\Omega_2=$ 2.24 eV) shows a characteristic double peak structure in the (Ω_3,Ω_2) signal representation. The $(2,2)\rightarrow(1,1)$ transitions of both the S_e-S_h and P_e-P_h channels are red shifted from

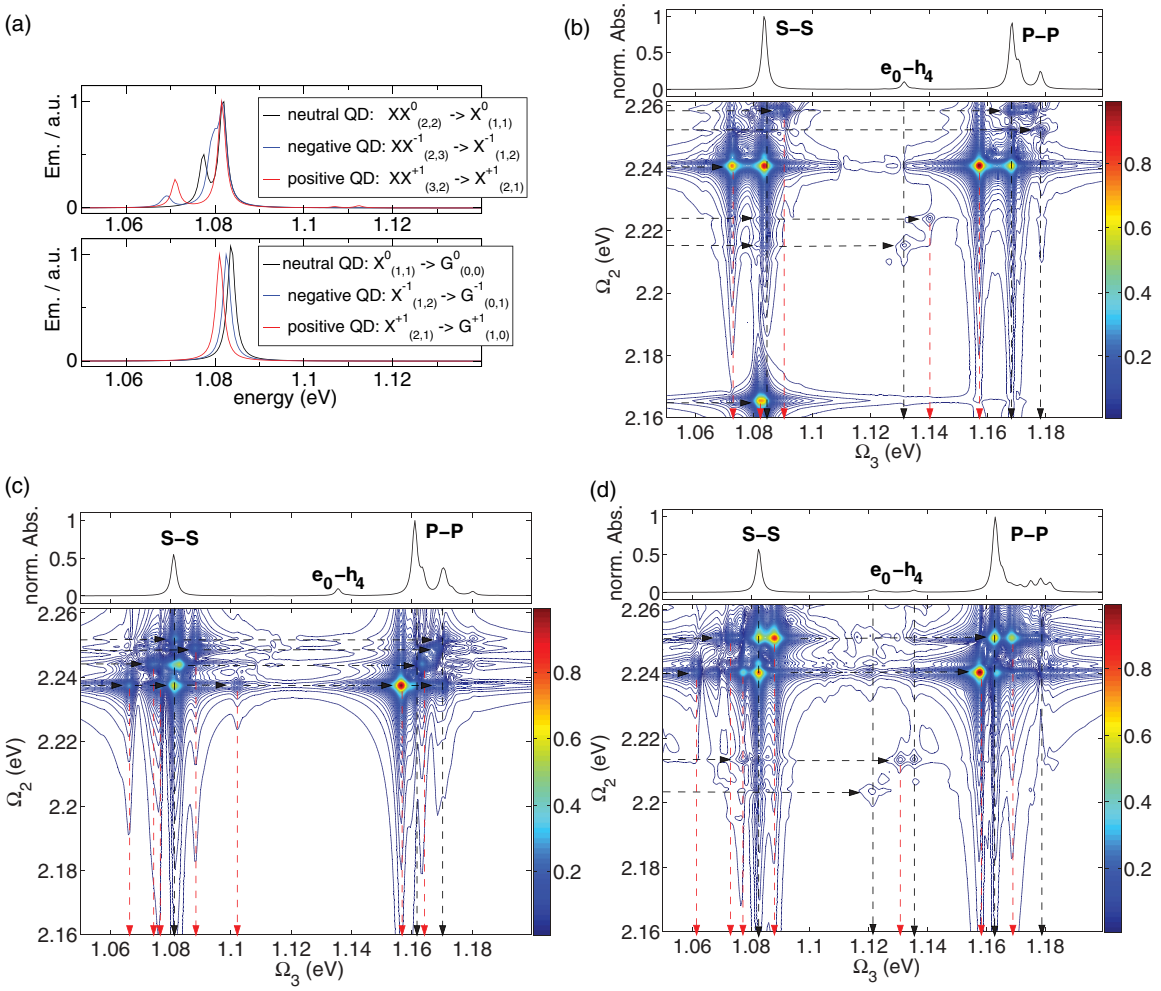

FIG. 4. (Color online) Simulated photoluminescence spectra (a) and simulated 2D double quantum coherence signals $S^{(3)}_{k_{\rm III}}(\Omega_3,\Omega_2,t_1)$ over Ω_3 and Ω_2 of a neutral (b), negatively (c), and positively charged quantum dot (d). The 2D-DQC signal is depicted as absolute value on a nonlinear scale defined by Eq. (8), $t_1 = 100$ fs.

the $(1,1) \rightarrow (0,0)$ fundamental. Furthermore, two additional weak XX^0 states appear at $\Omega_2 = 2.222$ and 2.259 eV in the $S^{(3)}_{k_{\rm III}}(\Omega_3,\Omega_2,t_1)$ signal, compared to the $S^{(3)}_{k_{\rm III}}(t_3,\Omega_2,\Omega_1)$ signal [see Fig. 3(b)]. The first one shows $S_e - S_h$ and $e_0 - h_4$ channel contributions, the latter one is composed of the $S_e - S_h$ and $P_e - P_h$ channels.

The 2D-DQC signal $S^{(3)}_{k_{\rm III}}(\Omega_3,\Omega_2,t_1)$ of the negatively and positively charged QDs reveals multipeak structures [see Figs. 4(c) and 4(d)]. The complex peak pattern arises from shifts of the $|XX^q\rangle \rightarrow |X^q\rangle$ resonances with respect to the $|X^q\rangle \rightarrow |G^q\rangle$ fundamentals. In contrast to the negative and neutral QD, where red shifted $|XX^q\rangle \rightarrow |X^q\rangle$ resonances dominate, the positively charged QD shows a strong contribution from a blue shifted $(3,2) \rightarrow (2,1)$ transitions of the $S_e - S_h$ channel ($\Omega_2 = 2.25$ eV).

C. Biexciton XX^q peak intensities

In contrast to linear absorption and emission signals [see Figs. 2 and 4(a)], the peak intensities in the 2D-DQC spectra [see Figs. 3 and 4(b)–4(d)] can be only inferred from the interference between the contributing pathways and are not related to a single transition moment. The imaginary part of both pahways ESA1 and ESA2 to the (Ω_3,Ω_2) signal is depicted in Fig. 5(a) for the neutral QD. The phase of both contributions leads to interference that defines the DQC signal intensity. The prominent double peak structure at $\Omega_2 = 2.24$ eV in the absolute value of the DQC signal [see Fig. 4(b)] can be decomposed into distinct contributions from both diagrams. Both ESA contributions are spectrally separated along the Ω_3 axis with the $(2,2) \rightarrow (1,1)$ resonances being red shifted by 11–12 meV from the $(1,1) \rightarrow (0,0)$ transitions in both the $S_e - S_h$ and $P_e - P_h$ channels. The lowest-energy biexciton $XX^0(\Omega_2 = 2.165$ eV) is composed solely of the $S_h - S_e$ channel, here the shift between $(1,1) \rightarrow (0,0)$ and $(2,2) \rightarrow (1,1)$ resonances is less pronounced (3 meV) but introduces the discussed asymmetry in the line shape of the total (Ω_3,Ω_2) signal. Cuts along the Ω_3 axis are depicted for the neutral, the negatively and positively charged QDs in Fig. 5(b) at the Ω_2 value of maximum peak intensity. In both charged QDs, the individual ESA contributions of the XX^{-1} and XX^{+1} states are spectrally resolved: the $S_e - S_h$ channel

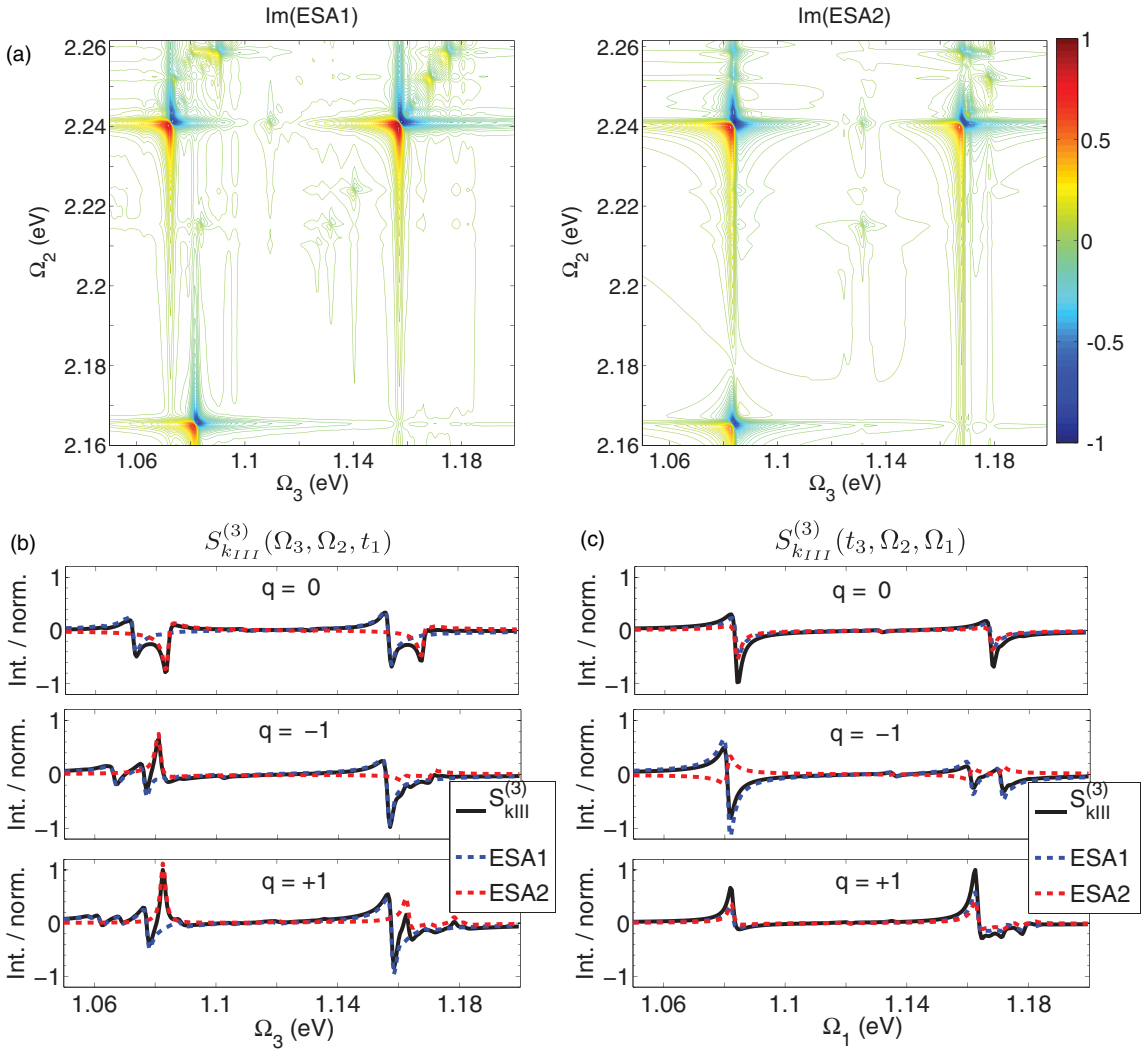

FIG. 5. (Color online) (a) Imaginary part of the ESA1 and ESA2 contributions to the 2D-DQC signal $S^{(3)}_{k_{III}}(\Omega_3,\Omega_2,t_1)$ of the neutral quantum dot, Eq. (7), $t_3 = 100$ fs. The signal is plotted on a nonlinear scale defined by Eq. (8). (b) Interfering pathways ESA1 and ESA2 for the $S^{(3)}_{k_{III}}(\Omega_3,\Omega_2,t_1)$ and the $S^{(3)}_{k_{III}}(t_3,\Omega_2,\Omega_1)$ (c) signals.

$((1,2) \rightarrow (0,1)$ and $(2,1) \rightarrow (1,0))$ is dominant in the ESA2 contribution. The $|XX^q\rangle \rightarrow |X^q\rangle$ transitions of the $P_e - P_h$ channel ($\Omega_3 \approx 1.16$ eV) dominate the ESA1.

Slices along Ω_1 are given in Fig. 5(c) for the (Ω_2,Ω_1) signal. In this signal representation, XX^q states are projected only on $|X^q\rangle \rightarrow |G^q\rangle$ transitions and the signal contributions ESA1 and ESA2 show up at the same Ω_1 frequency. In the neutral and positively charged QD [see Fig. 5(c), top and bottom], the ladder diagrams ESA1 and ESA2 add up constructively and the XX^0 state shows predominant contributions from the $S_e - S_h$ configuration ($\Omega_1 = 1.083$ eV) but weaker from the $P_e - P_h$ channel ($\Omega_1 = 1.169$ eV). For the XX^{+1} state, the importance of configurations is inverted and the $P_e - P_h$ configuration becomes dominant ($\Omega_1 = 1.163$ eV). In contrast, in the negatively charged QD [see Fig. 5(c), middle], both ladder diagrams add up with opposite phases defining the the XX^{-1} intensity. The presented slices along the monoexciton axis (Ω_1 or Ω_3) reveal the pronounced differences between QD's CI wave function compositions of the quantum states. This allows to decipher the underlying mechanism of the signal intensity, modulation of peak shapes and the occurrence of double peak structures in 2D-DQC signals on a fundamental level.

IV. CONCLUSIONS

We have simulated two projections of the 2D-DQC spectra [(Ω_2,Ω_1) and (Ω_3,Ω_2) representations] of QDs in different charged states. Both reveal only the biexciton XX^q energies along the Ω_2 axis that corresponds to the Fourier transform of the waiting time t_2 between the second and third laser pulse. Their constituent single-excitons X^q show up as resonances along the Ω_1 or Ω_3 axis revealing the multiconfiguration character of biexcitons XX^q. The simulations demonstrate, that different charged states of the QD lead to modulations in 2D-DQC peak pattern directly reflecting the dominant configurations to the CI wave function of biexcitons XX^q. Only in the neutral QD the lowest biexciton state XX^0 is projected exclusively on the $S_e - S_h$ channel as single contributing CI configuration. In the charged QDs, the Pauli blocking due

to partially occupied electron or hole states eliminates this low-energy XX^q resonance with exclusive $S_e - S_h$ character. All biexcitons of charged QD show strong configuration interactions in the XX^q wave functions with more than one leading configuration from $S_e - S_h$ and $P_e - P_h$ channels revealing the strong high-order electron correlation within the QDs. In the $S^{(3)}_{k_{\rm III}}(\Omega_3,\Omega_2,t_1)$ representation, the neutral QD XX^0 states show a double peak structure, which is assigned to $|X^0\rangle \rightarrow |G^0\rangle$ and red shifted $|XX^0\rangle \rightarrow |X^0\rangle$ resonances as doorway transitions to biexcitons XX^0. In the negatively charged QD multiple $|X^-\rangle$ states act as doorway transitions to XX^- with red shifted $|XX^-\rangle \rightarrow |X^-\rangle$ resonances, whereas a XX^{+1} biexciton constituent from blue shifted $|XX^+\rangle \rightarrow |X^+\rangle$ frequencies is identified.

In contrast to the linear optical signals, the intensity of 2D-DQC peaks results from the interference of density matrix diagrams, and may not be attributed to single transition moments. We find pronounced differences for the three charged states of the QDs with a destructive interference mechanism in the negatively charged QD and constructive interference in the neutral and positive QDs. In the (Ω_3,Ω_2) signal, the resonances of the individual pathways are spectrally resolved, which leads to the occurrence of the double peaks in the 2D-DQC signals.

We have demonstrated theoretically that the coherent third-order DQC technique can distinguish the quantum state of individual QDs and directly extract information about the wave function composition of the biexciton manifold XX^q, not accessible from linear spectroscopy. Optical signatures of different charged QD (neutral, negatively charged, and positively charges) in 2D-DQC spectra where identified. Multidimensional DQC spectroscopy (or 2D phase modulated fluorescence analogues) may serve as a particularly suitable tool for recording the charging state of single QD devices in operation and open the route for nonlinear spectroscopy with entangled photons.

ACKNOWLEDGMENTS

We gratefully acknowledge the support of the National Science Foundation through Grant No. CHE-1058791 and CHE-0840513, the Chemical Sciences, Geosciences and Biosciences Division, Office of Basic Energy Sciences, Office of Science, US Department of Energy and the Defense Advanced Research Projects Agency (DARPA), Grant UOFT-49606. B. P. F. and M. R. gratefully acknowledge support from the Alexander-von-Humboldt Foundation through the Feodor-Lynen program. M. R. also acknowledges financial support by the Deutsche Forschungsgemeinschaft through SFB 787. The work did by J. W. L. and A. Z. was funded by the US Department of Energy, Office of Science, Basic Energy Science, Materials Sciences and Engineering, under Contract No. DE-AC36-08GO28308 to NREL.

APPENDIX: SUM-OVER-STATES (SOS) EXPRESSION FOR THE 2D DOUBLE-QUANTUM-COHERENCE (2D-DQC) SIGNAL

Heterodyne detection is the most advanced detection method allowing to measure amplitude and phase of the DQC signal. The third-order heterodyne detected DQC signal $S^{(3)}_{k_{\rm III}}(t_3,t_2,t_1)$ depends parametrically on the delays between the laser pulses. The last pulse E_4 serves as a local oscillator field used for the heterodyne detection mode. Assuming that all pulses are temporally separated and phase matching conditions ($\mathbf{k}_{\rm III} = \mathbf{k_1} + \mathbf{k_2} - \mathbf{k_3}$), the contributions to $S^{(3)}_{k_{\rm III}}$ are given by two excited state (ESA) type ladder diagrams [see Figs. 3(a,iii) and 3(a,iv)]:

$$S^{(3)}_{k_{\rm III}}(t_3,\Omega_2,\Omega_1) = S^{(\rm ESA1)}_{k_{\rm III},i}(t_3,\Omega_2,\Omega_1) - S^{(\rm ESA2)}_{k_{\rm III},ii}(t_3,\Omega_2,\Omega_1). \tag{A1}$$

Here, we use a mixed time-frequency representation by performing a double-Fourier transform for t_1 and t_2. Both contributions to the 2D-DQC signal are given by the closed sum-over-state expressions derived in detail in Ref. 27:

$$\begin{aligned} &S^{(3)}_{k_{\rm III},i}(t_3,\Omega_2,\Omega_1) \\ &= \sum_{fee'g'} [\mu^*_{fe'}\, E^*_4(\omega_{fe'} - \omega_4)][\mu^*_{eg'}\, E^*_3(\omega_{eg'} - \omega_3)] \\ &\quad \times \frac{[\mu_{fe}\, E_2(\omega_{fe} - \omega_2)][\mu_{eg_0}\, E_1(\omega_{eg_0} - \omega_1)]}{\hbar^3(\Omega_2 - \xi_{fg_0})(\Omega_1 - \xi_{eg_0})} e^{-\imath\xi_{fe'}t_3}, \end{aligned} \tag{A2}$$

$$\begin{aligned} &S^{(3)}_{k_{\rm III},ii}(t_3 = 0+,\Omega_2,\Omega_1) \\ &= \sum_{fee'} [\mu^*_{e'g_0}\, E^*_4(\omega_{e'g_0} - \omega_4)][\mu^*_{fe'}\, E^*_3(\omega_{fe'} - \omega_3)] \\ &\quad \times \frac{[\mu_{fe}\, E_2(\omega_{fe} - \omega_2)][\mu_{eg_0}\, E_1(\omega_{eg_0} - \omega_1)]}{\hbar^3(\Omega_2 - \xi_{fg_0})(\Omega_1 - \xi_{eg_0})} e^{-\imath\xi_{e'g_0}t_3}. \end{aligned} \tag{A3}$$

Here, g denotes the ground state manifold of the QD $|G^q\rangle$, g_0 is the initially occupied lowest energy state $|G^q_0\rangle$ of the QD, e denotes single-excitons $|X^q\rangle$, f are biexcitons $|XX^q\rangle$, and $\xi_{ij} = \omega_i - \omega_j - \imath\gamma$. The phenomenological dephasing linewidth γ is assumed to be equal for all exciton transitions and reflects the width of sidebands of the QDs due to acoustical phonons[16,49–52] and the similar radiative exciton lifetimes of single- and biexcitons in single QD.[53,54] The spectral pulse envelopes

$$E(\omega) = \int \mathrm{d}t \exp(\imath\omega t) E(t) \tag{A4}$$

select possible transitions allowed by their bandwidth and thus serve as frequency filers that remove all transitions outside the bandwidth. In the simulations, we assume that the pulse bandwidth is larger than the exciton bandwidth, the impulsive signal then coincides with the third-order response function of the QD.

*alex.zunger@gmail.com
†smukamel@uci.edu

[1] O. E. Semonin, J. M. Luther, S. Choi, H.-Y. Chen, J. Gao, A. J. Nozik, and M. C. Beard, Science **334**, 1530 (2011).

[2]J. T. Stewart, L. A. Padilha, M. M. Qazilbash, J. M. Pietryga, A. G. Midgett, J. M. Luther, M. C. Beard, A. J. Nozik, and V. I. Klimov, Nano Lett. **12**, 622 (2012).
[3]D. Loss and D. P. DiVincenzo, Phys. Rev. A **57**, 120 (1998).
[4]P. Bhattacharya, S. Ghosh, and A. Stiff-Roberts, Annu. Rev. Mater. Res. **34**, 1 (2004).
[5]P. Michler, A. Kiraz, C. Becher, W. V. Schoenfeld, P. M. Petroff, L. Zhang, E. Hu, and A. Imamoglu, Science **290**, 2282 (2000).
[6]A. J. Shields, Nat. Photon. **1**, 215 (2007).
[7]C. Kindel, S. Kako, T. Kawano, H. Oishi, Y. Arakawa, G. Hönig, M. Winkelnkemper, A. Schliwa, A. Hoffmann, and D. Bimberg, Phys. Rev. B **81**, 241309 (2010).
[8]N. Akopian, N. H. Lindner, E. Poem, Y. Berlatzky, J. Avron, D. Gershoni, B. D. Gerardot, and P. M. Petroff, Phys. Rev. Lett. **96**, 130501 (2006).
[9]A. Schliwa, M. Winkelnkemper, A. Lochmann, E. Stock, and D. Bimberg, Phys. Rev. B **80**, 161307 (2009).
[10]F. Sotier, T. Thomay, T. Hanke, J. Korger, S. Mahapatra, A. Frey, K. Brunner, R. Bratschitsch, and A. Leitenstorfer, Nat. Phys. **5**, 352 (2009).
[11]C. L. Salter, R. M. Stevenson, I. Farrer, C. A. Nicoll, D. A. Ritchie, and A. J. Shields, Nature (London) **465**, 594 (2010).
[12]A. Mohan, M. Felici, P. Gallo, B. Dwir, A. Rudra, J. Faist, and E. Kapon, Nat. Photon. **4**, 302 (2010).
[13]R. J. Warburton, C. Schaflein, D. Haft, F. Bickel, A. Lorke, K. Karrai, J. M. Garcia, W. Schoenfeld, and P. M. Petroff, Nature (London) **405**, 926 (2000).
[14]M. Bayer, O. Stern, P. Hawrylak, S. Fafard, and A. Forchel, Nature (London) **405**, 923 (2000).
[15]*Optical Properties of Semiconductor Quantum Dots*, edited by U. Woggon (Springer, Berlin, 1997).
[16]P. Borri, W. Langbein, S. Schneider, U. Woggon, R. L. Sellin, D. Ouyang, and D. Bimberg, Phys. Rev. Lett. **87**, 157401 (2001).
[17]V. Mlinar and A. Zunger, Phys. Rev. B **80**, 035328 (2009).
[18]J. Kim, S. Mukamel, and G. D. Scholes, Acc. Chem. Res. **42**, 1375 (2009).
[19]K. W. Stone, K. Gundogdu, D. B. Turner, X. Li, S. T. Cundiff, and K. A. Nelson, Science **324**, 1169 (2009).
[20]S. T. Cundiff, J. Opt. Soc. Am. B **29**, A69 (2012).
[21]G. Moody, M. E. Siemens, A. D. Bristow, X. Dai, A. S. Bracker, D. Gammon, and S. T. Cundiff, Phys. Rev. B **83**, 245316 (2011).
[22]C. Scheurer and S. Mukamel, J. Chem. Phys. **115**, 4989 (2001).
[23]S. Mukamel, R. Oszwaldowski, and D. Abramavicius, Phys. Rev. B **75**, 245305 (2007).
[24]S. Mukamel, R. Oszwaldowski, and L. Yang, J. Chem. Phys. **127**, 221105 (2007).
[25]D. B. Turner, P. Wen, D. H. Arias, and K. A. Nelson, Phys. Rev. B **84**, 165321 (2011).
[26]Y. Benny, Y. Kodriano, E. Poem, D. Gershoni, T. A. Truong, and P. M. Petroff, Phys. Rev. B **86**, 085306 (2012).
[27]D. Abramavicius, B. Palmieri, D. V. Voronine, F. Šanda, and S. Mukamel, Chem. Rev. **109**, 2350 (2009).
[28]M. Richter, F. Schlosser, M. Schoth, S. Burger, F. Schmidt, A. Knorr, and S. Mukamel, Phys. Rev. B **86**, 085308 (2012).
[29]P. Tian, D. Keusters, Y. Suzaki, and W. S. Warren, Science **300**, 1553 (2003).
[30]M. F. Gelin, D. Egorova, and W. Domcke, Acc. Chem. Res. **42**, 1290 (2009).
[31]M. Cho, N. F. Scherer, G. R. Fleming, and S. Mukamel, J. Chem. Phys. **96**, 5618 (1992).
[32]T. J. Dunn, I. A. Walmsley, and S. Mukamel, Phys. Rev. Lett. **74**, 884 (1995).
[33]J. A. Cina, Annu. Rev. Phys. Chem. **59**, 319 (2008).
[34]G. A. Lott, A. Perdomo-Ortiz, J. K. Utterback, A. Aspuru-Guzik, and A. H. Marcus, Proc. Natl. Acad. Sci. USA **108**, 16521 (2011).
[35]S. Mukamel and M. Richter, Phys. Rev. A **83**, 013815 (2011).
[36]P. F. Tekavec, T. R. Dyke, and A. H. Marcus, J. Chem. Phys. **125**, 194303 (2006).
[37]P. F. Tekavec, G. A. Lott, and A. H. Marcus, J. Chem. Phys. **127**, 214307 (2007).
[38]D. Brinks, F. D. Stefani, F. Kulzer, R. Hildner, T. H. Taminiau, Y. Avlasevich, K. Müllen, and N. F. van Hulst, Nature (London) **465**, 905 (2010).
[39]M. Ediger, G. Bester, A. Badolato, P. M. Petroff, K. Karrai, A. Zunger, and R. J. Warburton, Nat. Phys. **3**, 774 (2007).
[40]A. Franceschetti, H. Fu, L. W. Wang, and A. Zunger, Phys. Rev. B **60**, 1819 (1999).
[41]L.-W. Wang and A. Zunger, Phys. Rev. B **59**, 15806 (1999).
[42]A. J. Williamson, L. W. Wang, and A. Zunger, Phys. Rev. B **62**, 12963 (2000).
[43]G. Bester, S. Nair, and A. Zunger, Phys. Rev. B **67**, 161306 (2003).
[44]J.-W. Luo, L. Zhang, and A. Zunger, Phys. Rev. B **84**, 121303 (2011).
[45]J.-W. Luo, A. N. Chantis, M. van Schilfgaarde, G. Bester, and A. Zunger, Phys. Rev. Lett. **104**, 066405 (2010).
[46]J.-W. Luo, G. Bester, and A. Zunger, Phys. Rev. Lett. **102**, 056405 (2009).
[47]J. W. Luo, A. Franceschetti, and A. Zunger, Phys. Rev. B **79**, 201301 (2009).
[48]J.-W. Luo, A. Franceschetti, and A. Zunger, Nano Lett. **9**, 2648 (2009).
[49]B. Krummheuer, V. M. Axt, and T. Kuhn, Phys. Rev. B **65**, 195313 (2002).
[50]J. Förstner, C. Weber, J. Danckwerts, and A. Knorr, Phys. Status Solidi B **238**, 419 (2003).
[51]B. Krummheuer, V. M. Axt, T. Kuhn, I. D'Amico, and F. Rossi, Phys. Rev. B **71**, 235329 (2005).
[52]E. Stock, M.-R. Dachner, T. Warming, A. Schliwa, A. Lochmann, A. Hoffmann, A. I. Toropov, A. K. Bakarov, I. A. Derebezov, M. Richter, V. A. Haisler, A. Knorr, and D. Bimberg, Phys. Rev. B **83**, 041304 (2011).
[53]G. Bacher, R. Weigand, J. Seufert, V. D. Kulakovskii, N. A. Gippius, A. Forchel, K. Leonardi, and D. Hommel, Phys. Rev. Lett. **83**, 4417 (1999).
[54]C. Santori, G. S. Solomon, M. Pelton, and Y. Yamamoto, Phys. Rev. B **65**, 073310 (2002).
[55]D. Abramavicius and S. Mukamel, J. Chem. Phys. **133**, 184501 (2010).
[56]V. Mlinar and A. Zunger, Phys. Rev. B **80**, 205311 (2009).